J. Fluid Mech. (2023), *vol*. 975, R3, doi:10.1017/jfm.2023.898

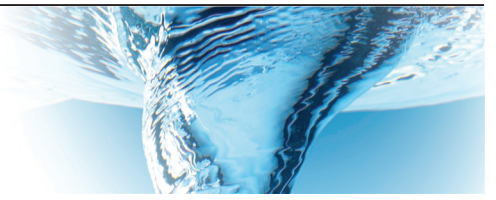

Minimum current for detachment of electrolytic bubbles

Yixin Zhang[1],† **and Detlef Lohse**[1,2]

[1]Physics of Fluids Group, Max Planck Center Twente for Complex Fluid Dynamics and J. M. Burgers Centre for Fluid Dynamics, University of Twente, P.O. Box 217, 7500 AE Enschede, The Netherlands

[2]Max Planck Institute for Dynamics and Self-Organization, 37077 Göttingen, Germany

(Received 29 September 2023; revised 23 October 2023; accepted 23 October 2023)

The efficiency of water electrolysis is significantly impacted by the generation of micro- and nanobubbles on the electrodes. Here molecular dynamics simulations are used to investigate the dynamics of single electrolytic nanobubbles on nanoelectrodes. The simulations reveal that, depending on the value of current, nucleated nanobubbles either grow to an equilibrium state or grow unlimitedly and then detach. To account for these findings, the stability theory for surface nanobubbles is generalized by incorporating the electrolytic gas influx at the nanobubble's contact line and adopting a real gas law, leading to accurate predictions for the numerically observed transient growth and stationary states of the nanobubbles. With this theory, the minimum current for bubble detachment can also be derived analytically. In the detachment regime, the radius of the nanobubble first increases with time (t) as $R \propto t^{1/2}$ and then as $R \propto t^{1/3}$, up to bubble detachment.

Key words: bubble dynamics

1. Introduction

Hydrogen produced by water electrolysis using gas-evolving electrodes from renewable electricity is essential for achieving carbon neutrality and a sustainable future (Brauns & Turek 2020; Yue *et al.* 2021; Shih *et al.* 2022). However, micro- and nanobubbles formed at an electrode can result in undesired blockage of the electrode and thus decrease the energy transformation efficiency (Vogt & Balzer 2005; Zhao, Ren & Luo 2019; Angulo *et al.* 2020). Addressing this problem requires a deeper understanding of the dynamics of individual nanobubbles on electrodes. Recent advancements in experimental techniques have enabled the generation of single electrolytic nanobubbles (Luo & White 2013;

† Email address for correspondence: y.zhang-11@utwente.nl

Liu *et al.* 2017; Edwards, White & Ren 2019). Though the formed single nanobubbles cannot be observed directly, their presence and equilibrium states are indicated by a sudden drop of the peak current to a steady value (Luo & White 2013; Liu *et al.* 2017; Edwards *et al.* 2019). Numerical methods such as finite element or difference methods (Luo & White 2013; Higuera 2021) and molecular dynamics simulations (Perez Sirkin *et al.* 2019; Maheshwari *et al.* 2020; Ma *et al.* 2021) have also been used to study the nucleation and stability mechanism of electrolytic nanobubbles. However, a fundamental theory for the statics and dynamics of single electrolytic nanobubbles is still lacking.

Electrolytic nanobubbles belong to the family of surface nanobubbles. Since their discovery in the 1990s, surface nanobubbles have triggered the fascination of scientists (Lohse & Zhang 2015*b*) due to their unique properties such as their long lifetime (Lou *et al.* 2000; Weijs & Lohse 2013) and their small contact angles (Zhang, Maeda & Craig 2006), and because of their practical relevance and applications in flotation (Calgaroto, Wilberg & Rubio 2014), nanomaterial engineering (Hui *et al.* 2009) and diagnostics (Batchelor *et al.* 2020). Significant progress has been made (see the reviews Lohse & Zhang 2015*b*; Tan, An & Ohl 2021) in developing new methods for generating and detecting nanobubbles, as well as clarifying their stability mechanism by an analytical model developed by Lohse & Zhang (2015*a*) (and extensions thereof), which suggests that a stable balance between the Laplace pressure-driven gas outflux and the local oversaturation-driven gas influx is made possible by contact line pinning.

This work aims to understand the dynamics of single electrolytic nanobubbles through molecular dynamics simulations and analytical theories. The Lohse–Zhang model is generalized to account for the gas produced at the contact line. The new model can quantitatively explain the conducted molecular simulations without any free parameters. This generalization thus creates a unified theoretical framework that can predict not only the equilibrium states of stable electrolytic nanobubbles (such as contact angles and the time required to reach equilibrium), but also the unbounded growth of unstable electrolytic nanobubbles, which eventually detach.

2. Molecular simulations

Molecular dynamics (MD) simulations are used as virtual experiments to simulate the generation of electrolytic nanobubbles on nanoelectrodes. We adopt the open-source code LAMMPS (Plimpton 1995). As shown in figure 1(*a*), the minimal molecular system consists of water molecules (represented in orange), gas atoms (in green), atoms of the electrode (in white), atoms of the solid base (in blue) and atoms of the 'piston' plate (in bronze). The water is modelled by the monoatomic water (mW) potential (Molinero & Moore 2009), implying a surface tension $\gamma = 66\,\mathrm{mN\,m^{-1}}$. Except for water itself, the intermolecular potentials U between i-type atoms and j-type atoms are simulated with the standard Lennard-Jones (LJ) 12-6 potential:

$$U(r_{ij}) = \begin{cases} 4\varepsilon_{ij}\left[\left(\dfrac{\sigma_{ij}}{r_{ij}}\right)^{12} - \left(\dfrac{\sigma_{ij}}{r_{ij}}\right)^{6}\right] & \text{if } r_{ij} \le r_c, \\ 0 & \text{if } r_{ij} > r_c, \end{cases} \tag{2.1}$$

where r_{ij}, ε_{ij}, σ_{ij} and r_c are the pairwise distance, energy parameter, length parameter and cutoff distance, respectively. The cutoff distance is chosen as $r_c = 16.5\,\text{Å}$. The complete list of parameters among the water (W), gas (G), electrodes (E), base solids (S) and piston (P) are given in table 1.

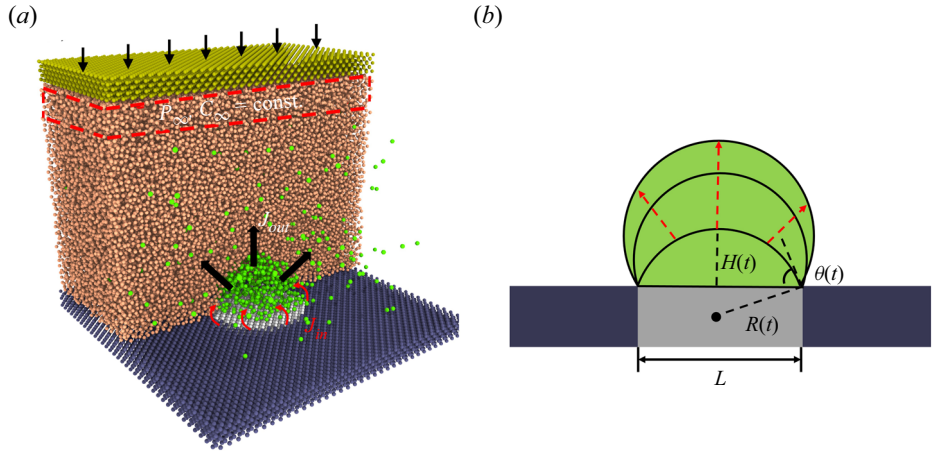

Figure 1. (*a*) A snapshot of the generated electrolytic nanobubble on the nanoelectrode in MD simulations. The simulated domain has been sliced to observe the bubble. The system's condition is maintained at temperature $T = 300$ K, pressure $P_\infty = 10$ atm and gas concentration $C_\infty = c_s$ (c_s is the gas solubility). The nanoelectrode has a diameter $L = 5.76$ nm and is made hydrophobic to water, while the surrounding solid is hydrophilic. Here J_{in} represents the gas influx to the bubble produced at the contact line, while J_{out} represents the diffusive outflux through the bubble interface. (*b*) Sketch of a growing bubble with pinning length L, contact angle $\theta(t)$, radius of curvature $R(t)$ and height $H(t)$.

Atom type	Atom type	ε_{ij} (kcal mol^{-1})	σ_{ij} (Å)
G	G	0.188	3.75
W	G	0.20	3.07
W	E	0.15	3.32
G	E	0.26	3.32
W	S	0.8	3.32
W	P	0.5	3.32
G	P	0.5	3.32

Table 1. Interaction parameters.

Note that the atoms of electrodes and base solids are fixed so that there is no need to specify the interactions among them. The atoms of the piston move in the same phase so that the interactions inside them are also ignored.

The gas modelled by the standard LJ 12-6 potential has a density $\rho_\infty = 11.47$ kg m^{-3} at 10 atm and 300 K. The molar mass of the gas is 28 g mol^{-1}. The gas–water interaction is tuned to obtain a gas solubility $c_s = 0.54$ kg m^{-3} (calculated using Henry's law) and a mass diffusivity $D = 4.1 \times 10^{-9}$ m^2 s^{-1} (calculated using Einstein relation (Skoulidas & Sholl 2005)). The electrochemical reaction that transforms water molecules into gas atoms is modelled in a simple way similar to previous MD studies (Perez Sirkin *et al.* 2019; Maheshwari *et al.* 2020; Ma *et al.* 2021) where right above the electrodes, two layers of water molecules can turn into gas atoms conducted at a fixed rate, leading to a constant gas influx J_{in}, i.e. a constant current i_{in} (assuming the production of each gas atom needs a specific number of electrons). Note that the contact line of the bubble is fluctuating so that there are still some water molecules available on the electrode after bubble formation

to ensure a constant J_{in}, which is the case for the simulations done in this work. However, for sufficiently large J_{in}, there can be a shortage of water molecules to keep a constant J_{in}.

By adjusting the water–electrode interaction ε_{we}, the electrode is made hydrophobic with a water contact angle of 120°. Conversely, the base solid is set to be hydrophilic to water with a contact angle of 5°. Such settings force the bubble to be pinned around the electrode.

The box has a fixed lateral size ($L_x = 17.28\,\text{nm}$, $L_y = 17.28\,\text{nm}$). The height of this box is adjusted to maintain the far-field pressure $P_\infty = 10\,\text{atm}$ where periodic boundary conditions are applied in the other two directions. The initial thickness of the water slab is 11.3 nm with 124 416 atoms. The thickness of the solid base is 0.96 nm and has a face-centred cubic (fcc) structure with a number density $0.0332\,\text{Å}^{-3}$. The far-field gas concentration is maintained at the gas solubility by switching the identity of gas atoms back into the identity of water atoms, performed in a box right below the piston. This process is carried out only when the gas concentration in the box is larger than the gas solubility.

As sketched in figure 1(*a*,*b*), after nucleation the bubble grows until the balance between the Laplace pressure-driven diffusive outfluxes (J_{out}) and the reaction-driven gas influxes (J_{in}) is achieved (which may not happen). The evolution of the bubble's contact angle $\theta(t)$, radius of curvature $R(t)$ and height $H(t)$ will be of particular interest in this study.

3. Results and discussions

We find that for very small gas influxes, no bubbles can nucleate due to the low level of oversaturation around the electrodes. The gas concentration in steady states close to the electrode may be estimated by $c_L = c_s + J_{in}/(2DL)$ (Saito 1968) so that a critical concentration for the bubble to nucleate requires a critical gas influx. In our simulations, for $J_{in} > 1 \times 10^{-15}\,\text{kg}\,\text{s}^{-1}$ (corresponding to approximately 100 times oversaturation), nucleation always happens in agreement with the critical oversaturation found in experiments (Chen *et al.* 2014). The initial contact angle θ_i for the pinned bubble may be estimated by assuming that the bubble is composed of one layer of gas atoms with height 0.375 nm and using the geometric relation $H = L(1 - \cos\theta)/(2\sin\theta) \approx L\theta/4$ results in $\theta_i = 15°$, which is very similar to the $\theta_i = 20°$ determined by the voltammetric method in experiments (Edwards *et al.* 2019). Such a small θ_i makes it possible to study the evolution of contact angles of nanobubbles.

Indeed, for example, in the case of $J_{in} = 1.86 \times 10^{-15}\,\text{kg}\,\text{s}^{-1}$, its MD snapshots in figure 2(*a*) (also see supplementary movie S1 available at https://doi.org/10.1017/jfm.2023.898) demonstrate the transient growth of the pinned nanobubble to its stationary state. The instantaneous contact angle $\theta(t)$ of the nanobubble is then obtained in the standard way (Zhang, Sprittles & Lockerby 2019; Weijs *et al.* 2011) by fitting the instantaneous liquid–gas interface with a spherical cap and is shown in figure 2(*a*) for three different gas influxes J_{in}. It can be seen that for all cases, $\theta(t)$ increases with time initially but reaches its steady state eventually. The equilibrated state can also be examined by tracking the number of gas atoms $N(t)$ in the bubble, shown in figure 2(*b*), which is obtained by counting the gas atoms below the instantaneous liquid–gas interface. After verifying that the nanobubbles are at equilibrium, the equilibrium contact angles θ_{eq} for different J_{in} are then obtained by averaging the data in the last 20 ns of each simulation and are shown in figure 3(*a*). For even larger gas influxes, e.g. $J_{in} = 4.5 \times 10^{-15}\,\text{kg}\,\text{s}^{-1}$, the nucleated nanobubble is unstable and it becomes so large that it comes

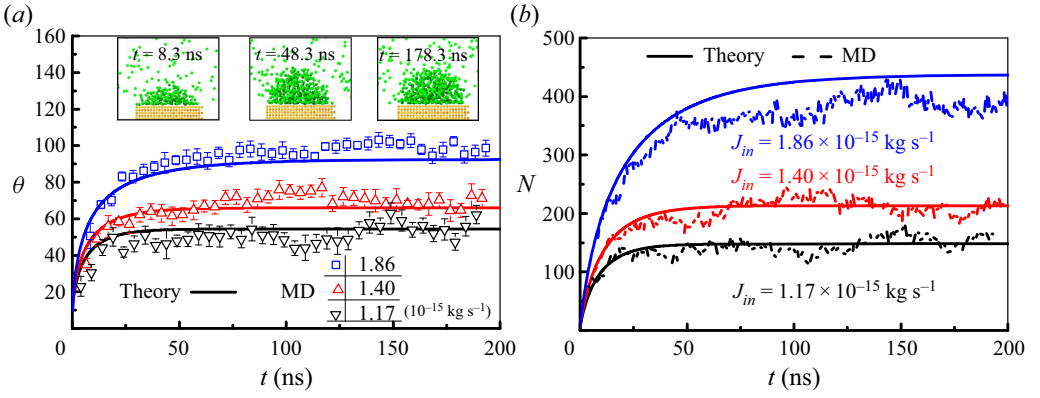

Figure 2. (*a*) Growth of contact angles to their equilibrium states for three different gas influxes J_{in} as given in the legend. The symbols represent MD results and solid lines are obtained by solving (3.5). The MD snapshots show the evolution of the simulated nanobubble for the case $J_{in} = 1.86 \times 10^{-15}$ kg s^{-1} at three different times. (*b*) Growth of the number of gas atoms in the bubble $N(t)$ to the equilibrium state for the same three different gas influxes.

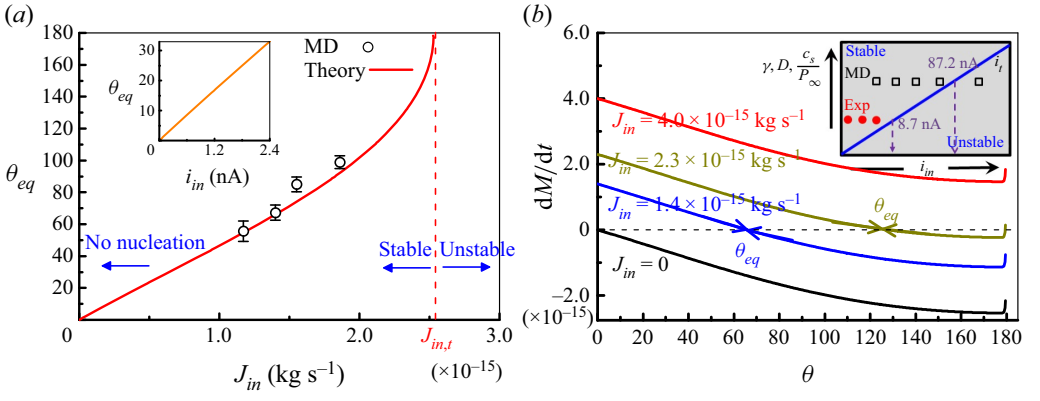

Figure 3. (*a*) The relation between equilibrium contact angles θ_{eq} and gas influx J_{in}. The symbols represent the results obtained from MD simulations. The solid line is the theoretical prediction, i.e. (3.8). Here J_t is the calculated threshold gas influx, differentiating between stable and unstable nanobubbles. The inset shows predictions for θ_{eq} of electrolytic bubbles in experiments (Liu *et al.* 2017) using the measured currents i_{in}, indicating that nanobubbles in experiments are indeed stable. (*b*) Dependence of the mass change rate on the contact angle for four different gas influxes. The inset shows a sketch of the phase diagram for stable and unstable nanobubbles observed in MD and experiments (Liu *et al.* 2017). The dividing line is given by the threshold current (3.10).

into contact with its periodic images in simulations, see figure 5(*a*) in the Appendix and supplementary movie S2.

3.1. *Generalized Lohse–Zhang equation*

To predict the transient growth and stationary states of electrolytic nanobubbles from MD simulations, we propose the following model. The longevity of surface nanobubbles is due to the contact line pinning and the local gas oversaturation as described by the Lohse–Zhang equation (Lohse & Zhang 2015*a*), derived in analogy to the problem of droplet evaporation (Popov 2005). After nucleation, the single electrolytic nanobubble

forming on the nanoelectrode gets pinned at the edge of the electrode due to the material heterogeneity between the electrode and the surrounding solid. The pinned nanobubble leads to the blockage of the water access to the electrode, leaving only the region of the bubble's contact line to produce gas. The produced gas J_{in} may enter directly into the bubble due to energy minimization. We reflect this in a generalization of the Lohse–Zhang equation in order to account for the gas production:

$$\frac{\mathrm{d}M}{\mathrm{d}t} = -\frac{\pi}{2}LDc_s\left(\frac{4\gamma}{LP_\infty}\sin\theta - \zeta\right)f(\theta) + J_{in}, \quad \text{with} \tag{3.1}$$

$$f(\theta) = \frac{\sin\theta}{1+\cos\theta} + 4\int_0^\infty \frac{1+\cosh 2\theta\xi}{\sinh 2\pi\xi}\tanh\left[(\pi-\theta)\,\xi\right]\,\mathrm{d}\xi. \tag{3.2}$$

Here J_{in} is the reaction-controlled gas influx at the contact line and is the new term as compared with the original Lohse–Zhang equation; M is the mass of the bubble; $\zeta = (c_\infty/c_s) - 1$ is the gas oversaturation and we choose the saturated situation $\zeta = 0$ as in real experiments and our simulations (ξ is the integral variable). The first term in the right-hand side of (3.1) is the diffusive outflux (J_{out}) through the bubble surface. Its relation with θ is shown in figure 3(b) (black solid line for $J_{in} = 0$).

The transient dynamics of the nanobubbles depends on the equation of state for gas atoms in the nanobubbles. For nanobubbles whose radii are as small as a few nanometres, the inside pressure P_R can be tens of millions of pascals (in our case, the maximum $P_R \approx 47$ MPa for $L = 5.76$ nm) so that the ideal gas law breaks down (see figure 5b in the Appendix). To account for the volume occupied by gas atoms and interatomic potentials, we adopt the Van der Waals equation as a real gas law, $N = PV/(Pb + k_BT)$ (Silbey *et al.* 2022), where N is the number of atoms, V is the total volume, $b = 4\pi\sigma_{eff}^3/3$ is the volume per atom with an effective atomic radius $\sigma_{eff} = 0.2$ nm, and k_B is the Boltzmann constant. Note that the modification to P by the interatomic interaction is included by the effective atomic radius. The bubble density thus is

$$\rho_R = \rho_\infty\left(1+\frac{2\gamma}{RP_\infty}\right)\frac{P_\infty b + k_BT}{\left(1+\dfrac{2\gamma}{RP_\infty}\right)P_\infty b + k_BT}. \tag{3.3}$$

Considering the bubble's volume is $V_b = \pi L^3(\cos^3\theta - 3\cos\theta + 2)/(24\sin^3\theta)$, we get

$$M = \frac{\rho_\infty\left(P_\infty b + k_BT\right)\left(\pi L^3\dfrac{\cos^3\theta - 3\cos\theta + 2}{24\sin^3\theta}\right)}{P_\infty b + \dfrac{k_BT}{1+\dfrac{4\gamma}{LP_\infty}\sin\theta}}. \tag{3.4}$$

Substituting (3.4) into (3.1) leads to an ordinary differential equation for $\theta(t)$:

$$\frac{\mathrm{d}\theta}{\mathrm{d}t} = \frac{-\dfrac{\pi}{2}LDc_s\left(\dfrac{4\gamma}{LP_\infty}\sin\theta - \zeta\right)f(\theta) + J_{in}}{\dfrac{\dfrac{\pi}{8}L^3\rho_\infty\left(P_\infty b + k_BT\right)}{\left(1+\dfrac{4\gamma}{LP_\infty}\sin\theta\right)P_\infty b + k_BT}(T_1 - T_2)}, \quad \text{with} \tag{3.5}$$

$$T_1 = \frac{1 + \dfrac{4\gamma}{LP_\infty}\sin\theta}{(1+\cos\theta)^2} + \frac{4\gamma}{LP_\infty}\frac{\cos^3\theta - 3\cos\theta + 2}{3\sin^3\theta}\cos\theta, \tag{3.6}$$

$$T_2 = \frac{\dfrac{4\gamma b}{L}\cos\theta\left(1 + \dfrac{4\gamma}{LP_\infty}\sin\theta\right)\left(\dfrac{\cos^3\theta - 3\cos\theta + 2}{3\sin^3\theta}\right)}{\left(1 + \dfrac{4\gamma}{LP_\infty}\sin\theta\right)P_\infty b + k_B T}. \tag{3.7}$$

The dynamical evolution of $\theta(t)$ and $N(t)$ are easily obtained by numerical solutions to (3.5). The results agree well with the results from the previous MD simulations (see solid lines in figure 2*a*,*b*).

3.2. *Threshold gas influx $J_{in,t}$ for stable and unstable nanobubbles*

The competition between the influx J_{in} and the outflux J_{out} leads to the possible existence of stable surface nanobubbles. As illustrated in figure 3(*b*), adding a small value of $J_{in} = 1.4 \times 10^{-15}\,\mathrm{kg\,s^{-1}}$ to $\mathrm{d}M/\mathrm{d}t$ allows the blue line to cross the horizontal dashed line of zero-mass change rate and the intersection point with the equilibrium angel θ_{eq} is indeed stable, as any deviations from θ_{eq} will lead to a mass flux bringing the angle back to θ_{eq} (see the arrows). Note that a further increase of the influx to $J_{in} = 2.3 \times 10^{-15}\,\mathrm{kg\,s^{-1}}$ leads to a bifurcation and two intersection points where $\mathrm{d}M/\mathrm{d}t = 0$ (see the bronze line), but only the first point is stable. By putting $\mathrm{d}M/\mathrm{d}t = 0$ in (3.1), we obtain an implicit expression for the equilibrium contact angle,

$$\sin\theta_{eq} f\left(\theta_{eq}\right) = \frac{P_\infty}{2\pi D c_s \gamma} J_{in}, \tag{3.8}$$

whose solutions for different J_{in} compare excellently with the equilibrium contact angles measured from MD simulations as shown in figure 3(*a*). To obtain an explicit equation for small contact angles, (3.8) can be simplified to $\theta_{eq} \approx J_{in}P_\infty/(8Dc_s\gamma)$. Practically this approximation works well for $\theta \leq \pi/2$. We also remark that for small gas influx J_{in} there is no bubble nucleation on the nanoelectrode but the exact value of the critical J_{in} for bubble nucleation is not explored in this work.

For large gas influxes, nanobubbles cannot be stable. This can be seen from figure 3(*b*) as adding a very large influx $J_{in} = 4.0 \times 10^{-15}\,\mathrm{kg\,s^{-1}}$ (see the red line) makes $\mathrm{d}M/\mathrm{d}t$ always positive (above the dashed line of zero-mass rate) for any angles so that no stable angles can exist. We also refer to figure 3(*a*) where no equilibrium angles can be obtained for $J_{in} > J_{in,t}$. The threshold influx $J_{in,t}$ differentiating stable nanobubbles from unstable nanobubbles is obtained as

$$J_{in,t} = \frac{2\pi\gamma D c_s}{P_\infty}\max[\sin\theta f\,(\theta)] \approx \frac{5.6\pi\gamma D c_s}{P_\infty}, \tag{3.9}$$

where the numerical value of $\max[\sin\theta f(\theta)] \approx 2.8$ has been used.

By multiplying $J_{in,t}$ with nF/M_g (n is the number of electrons transferred for each gas atom, F is the Faraday constant and M_g is the gas molar mass), the minimum (threshold) electric current for unstable nanobubbles is

$$i_t \approx \frac{5.6\pi\gamma D c_s n F}{P_\infty M_g}. \tag{3.10}$$

One can see from (3.10) and the phase diagram in the inset of figure 3(*b*) that electrolytic nanobubbles are more likely to be unstable for electrolytes with lower surface tension and

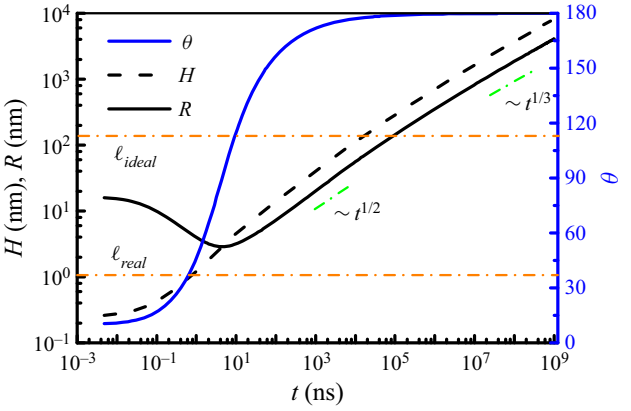

Figure 4. Unbounded growth of nanobubbles when the gas influx $J_{in} = 5.2 \times 10^{-15}\,\mathrm{kg\,s^{-1}}$ is beyond the threshold influx $J_{in,t} = 2.53 \times 10^{-15}\,\mathrm{kg\,s^{-1}}$. For $\ell_{real} \ll R \ll \ell_{ideal}$, the scaling $R \sim t^{1/2}$ is found while for $R \gg \ell_{ideal}$, $R \sim t^{1/3}$.

gas with lower mass diffusivity and solubility, since the corresponding threshold current (influx) is smaller.

Beyond this threshold influx ($J_{in,t} = 2.53 \times 10^{-15}\,\mathrm{kg\,s^{-1}}$, corresponding to $i_t = 87.2\,\mathrm{nA}$ for our simulations assuming $n = 1$), the nucleated nanobubble becomes unstable and can grow without bounds up to detachment from the electrode by buoyancy. Through the numerical solutions to (3.5) and using $R = L/(2\sin\theta)$ and $H = L(1-\cos\theta)/(2\sin\theta)$, figure 4 shows the evolution of the bubble's θ, R and H for the case $J_{in} = 5.2 \times 10^{-15}\,\mathrm{kg\,s^{-1}}$. It can be seen that after a specific time, the bubble grows with a contact angle approaching 180°, a constant net influx ($J_{in} + J_{out}$), and a fully spherical shape (not only a cap) whose volume is $\frac{4}{3}\pi R^3$. Therefore, the growth of the bubble is governed by $\mathrm{d}(\frac{4}{3}\pi R^3 \rho_R)/\mathrm{d}t = \text{const}$. The gas law (3.3) determines two length scales, $\ell_{ideal} = 2\gamma/P_\infty$ and $\ell_{real} = 2\gamma b/(k_B T)$. For a large bubble $R \gg \ell_{ideal}$, ρ_R is constant so that we have the usual 'reaction-controlled' scaling (Van Der Linde *et al.* 2017) for the bubble growth:

$$R \sim t^{1/3}, \quad \text{for } R \gg \ell_{ideal}. \tag{3.11}$$

However, for nanobubbles whose sizes can lie between $\ell_{real} \ll R \ll \ell_{ideal}$, the gas density is $\rho_R \sim R^{-1}$ so that one can obtain

$$R \sim t^{1/2}, \quad \text{for } \ell_{real} \ll R \ll \ell_{ideal}. \tag{3.12}$$

Interestingly, but incidentally, this new scaling $R \sim t^{1/2}$ is the same as that in the 'diffusion-controlled' growth of bubbles (Van Der Linde *et al.* 2017). But it is obvious that the nanobubbles studied here are always reaction-controlled. For $R \ll \ell_{real}$, the gas density is constant again but the pinned bubble is only a spherical cap. As the life cycle of an unstable nanobubble after birth can involve both regimes $\ell_{real} \ll R \ll \ell_{ideal}$ and $R \gg \ell_{ideal}$, the growth of the nanobubble experiences a transition from $R \sim t^{1/2}$ to $R \sim t^{1/3}$, as shown in figure 4. In this work, $\ell_{ideal} = 130\,\mathrm{nm}$ and $\ell_{real} = 1.0\,\mathrm{nm}$ (for $P_\infty = 10\,\mathrm{atm}$), so that the applicable region of the scaling $R \sim t^{1/2}$ is narrow. However, if $P_\infty = 1\,\mathrm{atm}$, $\ell_{ideal} = 1300\,\mathrm{nm}$, leading to a much wider region to observe $R \sim t^{1/2}$.

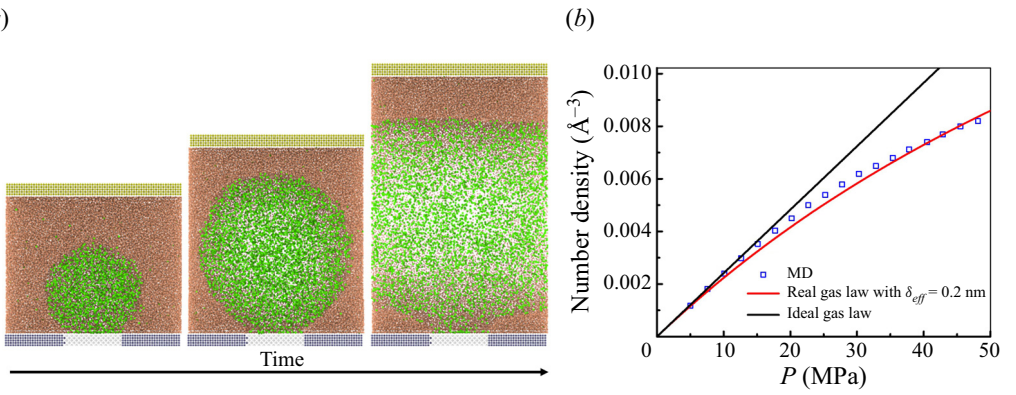

Figure 5. (*a*) The growth of unstable nanobubbles using $J_{in} = 4.5 \times 10^{-15}$ kg s^{-1}. (*b*) Equation of states measured from MD simulations (squares) in comparison with the ideal (black line) and real (red line) gas laws.

3.3. *Connections with experiments*

The work of White's group has focused on generating single surface nanobubbles on nanoelectrodes with radii < 50 nm (Luo & White 2013; Liu *et al.* 2017; Edwards *et al.* 2019). Unfortunately, direct visual observation of the evolving shape of nanobubbles is not possible due to technical and principal limitations. Based on the experimental data, the (constant) residual currents are 0.2–2.4 nA for different conditions (Liu *et al.* 2017), which translates into hydrogen influxes ranging from 2.08×10^{-18} kg s^{-1} to 24.96×10^{-18} kg s^{-1}. Using the water surface tension 72 mN m^{-1}, hydrogen solubility 1.6×10^{-3} kg m^{-3} and mass diffusivity 4.5×10^{-9} m^2 s^{-1} (Cussler 2009), the calculated contact angles based on our newly developed theory are between 3° and 33° (also see the inset of figure 3*a*), indicating that the generated nanobubbles are indeed stable. Note that the threshold current in experiments is calculated to be 8.7 nA and the experimental and MD results can be put together in the phase diagram in the inset of figure 3(*b*). The predicted small contact angles also agree with another experiment of electrolytic nanobubbles on highly ordered pyrolytic graphites (Yang *et al.* 2009).

4. Conclusions

In summary, the stability mechanism of electrolytic nanobubbles on nanoelectrodes has been explained by molecular simulations and the generalized Lohse–Zhang equation. The evolution of nanobubbles in molecular simulations can be nicely predicted by the new theory. We show that a minimum current (gas influx) is needed for nucleated nanobubbles to grow boundlessly so that they can detach from electrodes. In terms of stable nanobubbles, the relation between equilibrium contact angles and gas influxes is derived. We hope that this numerical and theoretical work will help develop improved methods to enhance bubble detachment and thus increase the efficiency of water electrolysis.

Supplementary movies. Supplementary movies are available at https://doi.org/10.1017/jfm.2023.898.

Acknowledgement. We are grateful for the discussions with A. Prosperetti.

Funding. We acknowledge the financial support by NWO under the project of ECCM KICKstart DE-NL.

Declaration of interests. The authors report no conflict of interest.

Author ORCIDs.
Yixin Zhang https://orcid.org/0000-0003-4632-3780;
Detlef Lohse https://orcid.org/0000-0003-4138-2255.

Appendix

For very large gas influx such as $J_{in} = 4.5 \times 10^{-15}\,\mathrm{kg\,s^{-1}}$, we find that the nanobubble grows quickly so that it comes into contact with its periodic image as shown in figure 5(*a*).

To obtain the relation between the gas density and pressure, we simulate a box containing 150 atoms in $\mathrm{NP_zT}$ (isothermal-isobaric) simulation. The $x = 2.4\,\mathrm{nm}$ and $y = 2.4\,\mathrm{nm}$ length of this box is fixed but the z length is allowed to move to control the pressure at the desired value. Figure 5(*b*) shows the obtained number density for different pressure from MD simulations (see squares). Clearly, when the pressure is larger than 20 MPa, the number density deviates from the prediction from the ideal gas law (black solid line). Thus the MD data are fitted by the real gas law and $\sigma_{eff} = 0.2\,\mathrm{nm}$ is obtained.

References

Angulo, A., van der Linde, P., Gardeniers, H., Modestino, M. & Rivas, D.F. 2020 Influence of bubbles on the energy conversion efficiency of electrochemical reactors. *Joule* **4** (3), 555–579.

Batchelor, D.V.B., Abou-Saleh, R.H., Coletta, P.L., McLaughlan, J.R., Peyman, S.A. & Evans, S.D. 2020 Nested nanobubbles for ultrasound-triggered drug release. *ACS Appl. Mater. Interfaces* **12** (26), 29085–29093.

Brauns, J. & Turek, T. 2020 Alkaline water electrolysis powered by renewable energy: a review. *Processes* **8** (2), 248.

Calgaroto, S., Wilberg, K.Q. & Rubio, J. 2014 On the nanobubbles interfacial properties and future applications in flotation. *Miner. Engng* **60**, 33–40.

Chen, Q., Luo, L., Faraji, H., Feldberg, S.W. & White, H.S. 2014 Electrochemical measurements of single H2 nanobubble nucleation and stability at Pt nanoelectrodes. *J. Phys. Chem. Lett.* **5** (20), 3539–3544.

Cussler, E.L. 2009 *Diffusion: Mass Transfer in Fluid Systems*. Cambridge University Press.

Edwards, M.A., White, H.S. & Ren, H. 2019 Voltammetric determination of the stochastic formation rate and geometry of individual H2, N2, and O2 bubble nuclei. *ACS Nano* **13** (6), 6330–6340.

Higuera, F.J. 2021 A model of the growth of hydrogen bubbles in the electrolysis of water. *J. Fluid Mech.* **927**, A33.

Hui, F., Li, B., He, P., Hu, J. & Fang, Y. 2009 Electrochemical fabrication of nanoporous polypyrrole film on HOPG using nanobubbles as templates. *Electrochem. Commun.* **11** (3), 639–642.

Liu, Y., Edwards, M.A., German, S.R., Chen, Q. & White, H.S. 2017 The dynamic steady state of an electrochemically generated nanobubble. *Langmuir* **33** (8), 1845–1853.

Lohse, D. & Zhang, X. 2015*a* Pinning and gas oversaturation imply stable single surface nanobubbles. *Phys. Rev.* E **91** (3), 031003(R).

Lohse, D. & Zhang, X. 2015*b* Surface nanobubbles and nanodroplets. *Rev. Mod. Phys.* **87** (3), 981.

Lou, S.-T., Ouyang, Z.-Q., Zhang, Y., Li, X.-J., Hu, J., Li, M.-Q. & Yang, F.-J. 2000 Nanobubbles on solid surface imaged by atomic force microscopy. *J. Vac. Sci. Technol.* **18** (5), 2573–2575.

Luo, L. & White, H.S. 2013 Electrogeneration of single nanobubbles at sub-50-nm-radius platinum nanodisk electrodes. *Langmuir* **29** (35), 11169–11175.

Ma, Y., Guo, Z., Chen, Q. & Zhang, X. 2021 Dynamic equilibrium model for surface nanobubbles in electrochemistry. *Langmuir* **37** (8), 2771–2779.

Maheshwari, S., Van Kruijsdijk, C., Sanyal, S. & Harvey, A.D. 2020 Nucleation and growth of a nanobubble on rough surfaces. *Langmuir* **36** (15), 4108–4115.

Molinero, V. & Moore, E.B. 2009 Water modeled as an intermediate element between carbon and silicon. *J. Phys. Chem.* B **113** (13), 4008–4016.

Perez Sirkin, Y.A., Gadea, E.D., Scherlis, D.A. & Molinero, V. 2019 Mechanisms of nucleation and stationary states of electrochemically generated nanobubbles. *J. Am. Chem. Soc.* **141** (27), 10801–10811.

Plimpton, S. 1995 Fast parallel algorithms for short-range molecular dynamics. *J. Comput. Phys.* **117** (1), 1–19.

Popov, Y.O. 2005 Evaporative deposition patterns: spatial dimensions of the deposit. *Phys. Rev.* E **71** (3), 036313.

SAITO, Y. 1968 A theoretical study on the diffusion current at the stationary electrodes of circular and narrow band types. *Rev. Polarogr.* **15** (6), 177–187.

SHIH, A.J., *et al.* 2022 Water electrolysis. *Nat. Rev. Meth. Primers* **2** (1), 84.

SILBEY, R.J., ALBERTY, R.A., PAPADANTONAKIS, G.A. & BAWENDI, M.G. 2022 *Physical Chemistry*. John Wiley & Sons.

SKOULIDAS, A.I. & SHOLL, D.S. 2005 Self-diffusion and transport diffusion of light gases in metal-organic framework materials assessed using molecular dynamics simulations. *J. Phys. Chem.* B **109** (33), 15760–15768.

TAN, B.H., AN, H. & OHL, C.-D. 2021 Stability of surface and bulk nanobubbles. *Curr. Opin. Colloid Interface Sci.* **53**, 101428.

VAN DER LINDE, P., MORENO SOTO, Á., PEÑAS-LÓPEZ, P., RODRÍGUEZ-RODRÍGUEZ, J., LOHSE, D., GARDENIERS, H., VAN DER MEER, D. & FERNÁNDEZ RIVAS, D. 2017 Electrolysis-driven and pressure-controlled diffusive growth of successive bubbles on microstructured surfaces. *Langmuir* **33** (45), 12873–12886.

VOGT, H. & BALZER, R.J. 2005 The bubble coverage of gas-evolving electrodes in stagnant electrolytes. *Electrochim. Acta* **50** (10), 2073–2079.

WEIJS, J.H. & LOHSE, D. 2013 Why surface nanobubbles live for hours. *Phys. Rev. Lett.* **110** (5), 054501.

WEIJS, J.H., MARCHAND, A., ANDREOTTI, B., LOHSE, D. & SNOEIJER, J.H. 2011 Origin of line tension for a Lennard–Jones nanodroplet. *Phys. Fluids* **23** (2), 022001.

YANG, S., TSAI, P., KOOIJ, E.S., PROSPERETTI, A., ZANDVLIET, H.J.W. & LOHSE, D. 2009 Electrolytically generated nanobubbles on highly orientated pyrolytic graphite surfaces. *Langmuir* **25** (3), 1466–1474.

YUE, M., LAMBERT, H., PAHON, E., ROCHE, R., JEMEI, S. & HISSEL, D. 2021 Hydrogen energy systems: a critical review of technologies, applications, trends and challenges. *Renew. Sust. Energy Rev.* **146**, 111180.

ZHANG, X.H., MAEDA, N. & CRAIG, V.S.J. 2006 Physical properties of nanobubbles on hydrophobic surfaces in water and aqueous solutions. *Langmuir* **22** (11), 5025–5035.

ZHANG, Y., SPRITTLES, J.E. & LOCKERBY, D.A. 2019 Molecular simulation of thin liquid films: thermal fluctuations and instability. *Phys. Rev.* E **100** (2), 023108.

ZHAO, X., REN, H. & LUO, L. 2019 Gas bubbles in electrochemical gas evolution reactions. *Langmuir* **35** (16), 5392–5408.